

An Observational Determination of the Proton to Electron Mass Ratio in the Early Universe ¹

Rodger I. Thompson

Steward Observatory, University of Arizona, Tucson, AZ 85721

`rit@email.arizona.edu`

Jill Bechtold

Steward Observatory, University of Arizona, Tucson, AZ 85721

`jbechtold@as.arizona.edu`

John H. Black

Onsala Space Observatory, Chalmers University of Technology, SE-43992 Onsala, Sweden

`John.Black@chalmers.se`

Daniel Eisenstein

Steward Observatory, University of Arizona, Tucson, AZ 85721

`deisenstein@as.arizona.edu`

Xiaohui Fan

Steward Observatory, University of Arizona, Tucson, AZ 85721

`fan@as.arizona.edu`

Robert C. Kennicutt

Institute of Astronomy, University of Cambridge, Cambridge CB3 0HA UK

`robk@ast.cam.ac.uk`

Steward Observatory, University of Arizona, Tucson, AZ 85721

Carlos Martins

Centro de Astrofísica, Universidade do Porto, Rua das Estrelas, 4150-762 Porto, Portugal

*Department of Applied Mathematics and Theoretical Physics, Centre for Mathematical
Sciences,*

University of Cambridge, Wilberforce Road, Cambridge CB3 0WA, United Kingdom

`C.J.A.P.Martins@damtp.cam.ac.uk`

J. Xavier Prochaska

Lick Observatory and University of California Santa Cruz, Santa Cruz, CA 95064

`xavier@ucolick.org`

and

Yancey L. Shirley

Steward Observatory, University of Arizona, Tucson, AZ 85721

`yshirley@as.arizona.edu`

ABSTRACT

In an effort to resolve the discrepancy between two measurements of the fundamental constant μ , the proton to electron mass ratio, at early times in the universe we reanalyze the same data used in the earlier studies. Our analysis of the molecular hydrogen absorption lines in archival VLT/UVES spectra of the damped Lyman alpha systems in the QSOs Q0347-383 and Q0405-443 yields a combined measurement of a $\Delta\mu/\mu$ value of $(-7 \pm 8) \times 10^{-6}$, consistent with no change in the value of μ over a time span of 11.5 gigayears. Here we define $\Delta\mu$ as $(\mu_z - \mu_0)$ where μ_z is the value of μ at a redshift of z and μ_0 is the present day value. Our null result is consistent with the recent measurements of King et al. (2009), $\Delta\mu/\mu = (2.6 \pm 3.0) \times 10^{-6}$, and inconsistent with the positive detection of a change in μ by Reinhold et al. (2006). Both of the previous studies and this study are based on the same data but with differing analysis methods. Improvements in the wavelength calibration over the UVES pipeline calibration is a key element in both of the null results. This leads to the conclusion that the fundamental constant μ is unchanged to an accuracy of 10^{-5} over the last 80% of the age of the universe, well into the matter dominated epoch. This limit provides constraints on models of dark energy that invoke rolling scalar fields and also limits the parameter space of Super Symmetric or string theory models of physics. New instruments, both planned and under construction, will provide opportunities to greatly improve the accuracy of these measurements.

Subject headings: cosmology:early universe

1. Introduction

The values of the fundamental constants determine the nature of the physical universe, from the size of mountains on earth to the eventual fate of the universe as a whole. Historically we have assumed that these constants are invariant in space and time. Speculation on the possibility of a time variation of the constants was first discussed by Dirac (1937), Teller (1948) and Gamow (1967). In very rare cases, such as the Oklo mine (Damour & Dyson 1996), there exists a terrestrial laboratory to test for time varying constants. It has been known for over thirty years (Thompson 1975) that Damped Lyman Alpha systems (DLAs) (Wolfe, Gawiser & Prochaska 2005) offer the opportunity to measure the value of the fundamental constant μ , the proton to electron mass ratio², at early times in the universe. The opportunity stems from the direct dependence of the rotational energy of molecules on μ and the square root dependency on μ of the vibrational energy relative to the electronic energy³. Each absorption line has a unique shift for a change in μ that depends on the vibrational and rotational quantum numbers of the upper and lower energy states. At the time of Thompson (1975), however, the observational capabilities of astronomical spectroscopy and the accuracy of molecular hydrogen laboratory spectroscopy allowed only very crude determinations of μ at relatively modest look back times. The high line density of atomic hydrogen lines in DLAs and the rarity of DLAs with measurable amounts of molecular hydrogen further complicated progress.

Foltz, Chaffee & Black (1988) and Cowie & Songaila (1995) made early measurements of μ at significant look back times and found no change to accuracies of $\Delta\mu/\mu \leq 2 \times 10^{-4}$ and 7×10^{-4} in the spectrum of PKS 0528-250 at a redshift of 2.811. At the same time calculations of the expected shifts were made by Varshalovich & Levshakov (1993) who developed a method of sensitivity constants for each line that will be discussed later in this work. An additional constraint of 2×10^{-4} was obtained on the same object by Potekhin et al. (1998).

¹Based on observations made with ESO Telescopes at the La Silla or Paranal Observatories under program IDs 68.A-0106 and 70.A-0017

²Although the literature is approximately equally divided in usage we designate μ as the proton to electron mass ratio rather than the inverse to be consistent with the other recent astronomical determinations of μ discussed here

³See Shu (1991) chapter 28 for an alternative derivation of the dependence

An excellent review of studies relevant to a determination of the time history of μ and other fundamental constants is given in Uzan (2003).

Three advances now provide the opportunity to measure μ at large look back times and at accuracies that are starting to impact other areas of physics such as dark energy and string theory. The first advance is the construction of large telescopes such as the Keck telescopes, the Very Large Telescopes (VLT) and now the Large Binocular Telescope (LBT). A second advance is the installation of stable, high resolution and sensitive spectrometers such as HIRES (Vogt et al. 1994) at Keck and UVES (Dekker et al. 2000) at the VLT. The third key advance is the measurement of the wavelengths of the H_2 Lyman and Werner electronic transitions to accuracies of a few parts in 10^8 (Ubachs et al. 2007). In addition Ubachs et al. (2007) has recalculated the sensitivity constants, taking into account both adiabatic and nonadiabatic perturbations, to provide an invaluable set of wavelengths at the present day value of μ and wavelength sensitivities to μ for the evaluation of the astronomical observations.

The most recent efforts to measure μ at high redshifts have centered on the Ultraviolet and Visible Echelle Spectrometer (UVES) on the VLT. The spectra of two quasars observed in January of 2002 (Q0347-383) and January of 2003 (Q0405-443) contain H_2 absorption lines at redshifts of 3.0249 and 2.5947. The first observations of Q0347-383 were commissioning observations carried out in 1999 and described by D’Odorico et al. (2001). Ivanchik et al. (2002) used this data along with a UVES spectrum of Q 1232+082 to investigate possible changes in μ . They found two results, $\Delta\mu/\mu = (5.7 \pm 3.8) \times 10^{-5}$ and $\Delta\mu/\mu = (12.5 \pm 4.5) \times 10^{-5}$ at the 3σ level for two different sets of Thorium Argon wavelength lists. A subsequent analysis by Levshakov et al. (2002) using just the Q0347-383 spectra found a result of $-1.5 \times 10^{-5} \leq \Delta\mu/\mu \leq 5.7 \times 10^{-5}$. A later reanalysis of the Q0347-382 data by Ivanchik et al. (2003) produced a limit at a confidence level of 95% of $|\Delta\mu/\mu| < 8 \times 10^{-5}$. Ubachs & Reinhold (2004) combined the line lists of Ivanchik et al. (2002) and Levshakov et al. (2002) and found that $\Delta\mu/\mu = (-0.5 \pm 3.6) \times 10^{-5}$ at the 2σ level.

The 2002 and 2003 UVES VLT observations of Q0347-383 and Q0405-443 (Ivanchik et al. 2005) had higher signal to noise than the 1999 observations. Using new laser determined H_2 wavelengths from Philip et al. (2004) and the UVES pipeline reduction of the spectra they found $\Delta\mu/\mu = (1.64 \pm 0.74) \times 10^{-5}$. Reinhold et al. (2006) subsequently utilized a new set of laser determined H_2 wavelengths and the pipeline data to find a change in μ of $\Delta\mu/\mu = (2.4 \pm 0.6) \times 10^{-5}$. Ubachs et al. (2007) details the determination of the H_2 parameters and gives a more complete list of laser determined wavelengths that slightly alters the result to $\Delta\mu/\mu = (2.45 \pm 0.59) \times 10^{-5}$. The Ubachs et al. (2007) H_2 parameters essentially remove the properties of H_2 from the error budget leaving the data reduction and signal to

noise of the observed spectrum as the primary error contributors. The Reinhold et al. (2006) result for Q0347-383 was examined by Wendt and Reimers (2008) who concluded that the data were consistent with $-0.7 \times 10^{-5} \leq \Delta\mu/\mu \leq 4.9 \times 10^{-5}$ at the 95% confidence level. King et al. (2009) have taken the same data set as Reinhold et al. (2006) with the addition of spectra of Q0528-250 and found a value of $\Delta\mu/\mu = (2.6 \pm 3.0) \times 10^{-6}$ for the combined data set. A key element in their analysis is an improved wavelength calibration as described in Murphy et al. (2008a). At this time there are two analyzes of the same data that lead to two different conclusions. Our independent analysis of the same data concludes that there is no evidence for a change in μ , consistent with the results of King et al. (2009).

For completeness we consider radio frequency measurements of μ that are more precise but at significantly lower redshift. Although the wavelength determinations are more precise, transitions in different molecules must be compared to provide information on any change in μ . Recently Flambaum & Kozlov (2007) have looked for variations in μ using the radio emission lines of ammonia and carbon monoxide. They take advantage of the high sensitivity of the inversion spectrum of ammonia to changes in μ with $\Delta\mu/\mu = 0.289 \frac{z_{inv} - z_{rot}}{1 + z_0}$ where z_{inv} is the redshift of the inversion lines of ammonia, z_{rot} is the redshift of the rotational lines of CO and z_0 is the cosmological redshift of the galaxy. For the galaxy B0218+357 at a redshift of 0.68470 they find $\Delta\mu/\mu = (0.6 \pm 1.9) \times 10^{-6}$. Murphy et al. (2008b) have improved this result to $\Delta\mu/\mu \leq 0.18 \times 10^{-6}$. This result is at relatively low redshift and it depends on ammonia and carbon monoxide having identical kinetic velocities in the molecular clouds. This is probably unlikely since, unlike the ubiquitous CO molecule, NH_3 is concentrated in the colder denser cores of molecular clouds. The fact that it is a null result, however, adds credence to the result since an offset in kinetic velocity would have to accurately match any change in μ to produce a null result. The result is also for a relatively low redshift, placing it within the current dark energy dominated epoch of the universe. Some dark energy theories predict that the fundamental constants only roll during the matter dominated epoch and freeze out at their present values once dark energy becomes dominant around a redshift of 1, (eg. Barrow, Sandvik & Magueijo (2002)). Table 1 provides a summary of the astronomical determinations of μ .

In our own galaxy Levshakov, Molaro & Kozlov (2008) have reported variations in μ based on the same ammonia transition along different lines of sight. In this case the variation is relative to the CCS molecule and is manifested by a general positive velocity offset between the ammonia and CCS emission lines. Their result gives $\Delta\mu/\mu = (4 - 14) \times 10^{-8}$. Slight errors in the line frequencies could mimic such a result.

Laboratory experiments have set limits on the present day rate of change of μ . Even though their time base is brief by cosmological standards, their wavelength accuracy is

far better than can be achieved in astronomical observations. The current best laboratory limits appear to be the results of Blatt et al. (2008) which give a result of $\dot{\mu}/\mu = (1.6 \pm 1.7) \times 10^{-15}/yr$. To put this in perspective if the rate of change is constant at $10^{-15}/yr$ then the change at the 11 gigayear look back time of Q0347-383 would be 1.1×10^{-5} , similar to the astronomical results given in this work. There is no real expectation that the rate of change would be constant so both the astronomical and laboratory results work in concert to constrain possible physical models that predict changes in time of the values of the fundamental constants. The results of Blatt et al. (2008) depend on the Schmidt model for the nuclear magnetic moment and therefore may be deemed as model dependent. A laboratory result that is independent of the Schmidt model is given by Shelkovnikov, Butcher, Chardonnet & Amy-Klein (2008) who give $\dot{\mu}/\mu = (-3.8 \pm 5.6) \times 10^{-14}/yr$. Other limits on the present rate of variation in μ based on the Weak Equivalence Principle and various theories of particle physics are discussed by Dent, Stern & Wetterich (2008).

The remainder of the paper addresses the measurement of μ in the spectra of Q0347-383 and Q0405-443. The wavelength calibration and data reduction to produce the spectra used in this work will only be summarized since it is discussed in detail in Thompson et al. (2009). That separate publication is intended to give a full description of the data analysis in order to allow the reader to concentrate on the measurement of μ described here without a lengthy data reduction description at the beginning. In this paper we bring those analysis methods to bear in an effort to discriminate between the positive and null results for a variation in μ .

2. Observations

The observations of Q0347-383 and Q0405-443 with UVES on VLT occurred during the nights of January 7-9 2002 for Q0347-383 and January 4-6 2003 for Q0405-443⁴. The emission line redshifts for these QSOs are 3.22 and 3.02 respectively (Ivanchik et al. 2005). The data were retrieved from the VLT archive along with the MIDAS based UVES pipeline reduction procedures. On each of the nights three separate spectra of the QSO were taken with accompanying long slit calibration lamp integrations at the same grating setting. The slit width and length for both object and calibration line observations are 0.8 and 6.6 arc seconds. The grating angle for the Q0347-383 observations had a central wavelength of 4300 Å and for Q0405-443, 3900 Å. The images are 2x2 pixel binned on chip with a size of 1024

⁴Based on observations made with ESO telescopes at the Paranal Observatory under program IDs 68.A-0106 and 70.A-0017

by 1500 binned pixels. A single pixel is 15 microns in size and 0.22 arc seconds on the sky. In the following the word pixel refers to the 2x2 binned pixels (0.44 arc seconds) in the images obtained from the archive. At 4000 Å a pixel is approximately 0.0416 Å which is about 3 km/sec. Both the calibration and object images are binned identically. Exposure times and other observational parameters are given in Tables 2 and 3 and are described in Ivanchik et al. (2005).

There are differences in the way the long slit calibration spectra were taken between the two objects. In the case of Q0405-443 there was a long slit calibration spectrum taken immediately after the object spectrum in all but one case. The time tags of the grating position encoder readouts for the object and calibration spectra are identical as are the values of the grating position encoder readings. This indicates that there was no adjustment of the grating position between the paired object and calibration spectra. The exception is the night of January 5, 2003 where there is no long slit calibration spectrum for the second object observation.

For Q0347-383 two long slit calibration spectra were taken in between the three object spectra for each night. The encoder readings indicate that there were no grating resets performed between the object spectrum and the calibration spectrum for the first two pairs of object and calibration observations for each night. The time tags, however, on the third night of January 10, 2002 pairs the long slit calibration spectrum with the third object spectrum. The proper pairings of observations are important in calculating the shifts needed to accurately combine the observations as is discussed in § 3.1.

3. Data Reduction

The spectra described by Ivanchik et al. (2005) and used by Reinhold et al. (2006) were produced by the standard UVES pipeline. The pipeline produces excellent spectra for most observations, however, Murphy et al. (2008a) points out that the Thorium Argon line list used in the wavelength calibration may not be accurate enough for the precise determination of fundamental constants. We reached similar conclusions as discussed in § 3.1. The final output of the UVES pipeline is an interpolated spectrum with equal wavelength intervals as opposed to an intensity and wavelength on a pixel by pixel basis. In what follows we only use images and spectra on a pixel by pixel basis. The wavelength calibration and the production of the spectra used in this study are described in detail in Thompson et al. (2009). The descriptions given here are short summaries of the methods.

3.1. Wavelength Calibration

Independently of Murphy et al. (2008a) we became aware that the standard Th/Ar line list used in the UVES pipeline analysis provides good wavelengths for most studies but is the primary limiting factor in obtaining the accuracy required for a determination of μ at the 10^{-5} level. In fact only about 1/4 of the lines are free of blending and other problems. We then recalibrated the wavelength solutions using the long slit calibration line spectra taken during the observations of the two QSOs. This is described in detail in Thompson et al. (2009) which is intended to serve as the record of the wavelength calibration used in this study and therefore will not be repeated here. The new wavelength calibration is the primary reason for a null result in this study. It should be noted that this recalibration differs from the recalibration used in King et al. (2009) in two ways. First, this calibration is based on the calibration spectra taken during the observation of the analyzed spectra. Second the calibration is done order by order. This results in some lines being declared good in one order but unusable in another order where they fall in low signal to noise areas.

The wavelength calibration described in Thompson et al. (2009) tracks the shifts in the wavelength positions between observations and between different observing nights. The final wavelength calibration is relative to a master solution which is set at a single position determined by a master long slit calibration lamp image that is the median of all of the calibration lamp images shifted to the position of the first calibration lamp image. The shifts are small, a few hundredths of a pixel width, but important in this study. The shifts are carried out by cubic interpolation and are rigid. The wavelength solution for each order of the master long slit calibration image is a six term Legendre polynomial whose coefficients are different for each order. The wavelength solution for the object spectra will differ from the master solution first due to small shifts in the actual grating position from the position appropriate to the master solution and due to the motion of the observatory about the barycenter of the earth-sun system. These are corrected for in the production of the individual spectra.

3.2. Spectrum Production

The order by order final spectrum for each object is a three dimensional array of dimensions [np,nord,6] where np is the number of pixels in the dispersion direction (1500), nord is the number of orders and the six last dimensions are flux, wavelength, variance, continuum, fit, and the fit convolved with the instrumental profile for each pixel in the spectrum. In this case the fit is the continuum minus the best fit to the H₂ lines at their natural line width. This is what the spectrum would look like if the instrument profile was infinitely narrow.

The first 2 are derived from the object and calibration spectra and calculated for each spectrum. The last 4 are calculated after the spectra are combined into a single spectrum but could be, in principle, calculated for the individual spectra. The observational parameters for Q0347-383 and Q0405-443 are listed in Tables 2 and 3 respectively.

3.2.1. *Flux*

At this stage there are 9 spectra for each of the 2 objects. In each order of the spectra the flux is distributed over several pixels in the cross dispersion direction. We tested several optimal extraction methods for combining the flux in the cross dispersion direction into a single value. These tests indicated that the UVES MIDAS V2.2.0 pipeline extraction did as good or better job of combining the flux than any of the methods we tested. We therefore used this intermediate product of the pipeline to produce the 9 flux versus pixel spectra for the 2 objects. These are not the interpolated to constant delta wavelength values spectra that are the final product of the pipeline. The next step is to assign a proper wavelength designation to each of the pixel positions in each order. Our goal is a proper vacuum wavelength at rest with respect to the barycenter of the earth sun system. Again note that our reference to pixels is to the 2x2 pixel binned output available in the archive.

3.2.2. *Wavelength*

As mentioned in § 3.1 the true wavelengths of the pixels are slightly different for each spectrum due to small shifts in the spectrometer configuration and different barycentric velocities. The wavelengths are calculated by first shifting the master wavelength solution by the amount calculated from the associated long slit calibration spectrum and then correcting the wavelengths for barycentric velocity. The associated long slit calibration line observations are given in Thompson et al. (2009).

The wavelength shift due to small differences in the grating position is calculated from the shifts found during the wavelength calibration. As described in § 2 care was taken to not reset the grating position between a long slit calibration observation and its associated object exposures. For these observations the shift of the object spectrum wavelength position is identical to the shift calculated for the associated calibration line spectrum given in Thompson et al. (2009). There are, however, two object observations where it appears that the grating position was reset without an associated long slit calibration line exposure. They are the observations in Table 2 for Q0347-383 that end in 109.b and 981.b. For these

observations our only recourse was to take the shift as the average between the shifts immediately preceding and immediately after the observations. The correlation between the encoder readouts and the shifts calculated during the wavelength calibration did not appear to be accurate enough to be used as a direct indicator of the amount of shift. Once the shift is determined the master wavelength solution is interpolated to account for the shift in pixel position between the associated calibration line image and the master image. The wavelengths associated with the flux in the pixels now have the correct observed vacuum wavelength as observed but must still be corrected for the barycentric velocity. Note that the handling of the shift values is different from the description given in Thompson et al. (2009). At that time it was not known that there was a procedure of resetting the grating position between observations. It does not affect the master wavelength calibration since the shifts were calculated directly from the calibration observations, but it does matter for the object spectra.

The component along the direction to the object of the barycentric velocity of the observatory was calculated using the date and time of the midpoint of the integration. This velocity is due to the earth’s orbit and rotation relative to the barycenter of the earth-sun system. The wavelength scale was then corrected for this motion so that the final wavelengths are vacuum wavelengths as observed in a reference frame at rest relative to the barycenter. This is slightly different than the heliocentric wavelengths used in Ivanchik et al. (2002).

3.3. Co-addition of the Spectra

At this point the individual spectra have the flux, wavelength and noise values populated in their respective arrays. The wavelengths, however, are slightly different for each spectrum due to the grating shifts and different barycentric velocities. Accurate co-addition of the spectra requires that they all be on the same wavelength scale. We choose to shift all of the spectra to the wavelength scale of the master wavelength solution for the grating angle setting as described in Thompson et al. (2009).

3.3.1. *Shift to Common Wavelength Scale*

The spectrum shift was accomplished by interpolation of the flux from the wavelength scale of the spectrum to the master wavelength scale of the master solution using the IDL⁵

⁵IDL stands for Interactive Data Language registered by ITT Visual Information Solutions

code procedure *INTERPOL* in double precision mode. In the following we will write IDL provided procedure names in capital italic letters and procedures written by the authors using IDL code in lower case italics. *INTERPOL* uses linear interpolation which is appropriate for this case since the shifts are only a few hundredths of a pixel. For cases with significant fractions of a pixel other interpolation methods may be more appropriate. At the end of this procedure all spectra are on a common wavelength scale, the master wavelength solution for each order.

3.3.2. *Addition of the Spectra*

All of the observed spectra for each of the two objects were combined to produce the final two spectra for analysis. The excellent and uniform observing conditions at the VLT produced a suite of individual spectra with remarkably similar signal to noise characteristics. In other words the weight of each of the spectra were essentially indistinguishable from each other. For this reason we simply produced two spectra for each object, one that is the mean of all the flux values at a given wavelength and the second which is the median of the flux values. Again the differences between these two spectra were minimal. The median spectrum was judged to have slightly better signal to noise in both objects and is the spectrum that is used in the analysis.

3.3.3. *The Variance*

The UVES pipeline calculates the variance for each of the spectrum fluxes but the documentation is not clear on the exact method of calculation. The variance is an important quantity in calculating the χ^2 values for the wavelength and density fits so uncertainty in how it was calculated is worrisome. The variance is therefore calculated explicitly from the 9 spectra normalized to a common total flux value. The normalizations varied between 0.8 and 1.2 for the 9 spectra that were combined to make the final spectrum for each object. The normalization, therefore, does not have a large effect on the calculated variance.

3.4. **H₂ Line Parameters**

A primary component of this study is the use of accurate molecular data provided by several recent studies of the H₂ molecule (Ubachs et al. (2007), Ivanov et al. (2008) and the references therein). The data from these references include the vacuum wavelengths and

calculated sensitivity factors K_i where the index i indicates the line. The sensitivity factor to a variation in μ is different for each line and is defined as

$$K_i = \frac{d \ln \lambda_i}{d \ln \mu} = \frac{\mu}{\lambda_i} \frac{d \lambda_i}{d \mu} \quad (1)$$

The precise vacuum wavelengths from these references have average errors on the order of 5×10^{-6} Å which produce a negligible contribution to the errors in determining the redshift of each line. The oscillator strengths for each transition were calculated using the Einstein A coefficients from Abgrall et al. (1993a) for the Lyman transitions and Abgrall et al. (1993b) for the Werner transitions.

3.5. Output Products

The calculation maintains two primary output products. The first is a six component spectrum of each order. The six components are the double precision wavelength, the flux, the standard deviation of the flux, the continuum fit, the line fit and the line fit convolved with the instrument profile. The second output is an IDL structure array which contains the line information. An IDL structure is a multi-format data set that can contain text, integer, floating point and arrays of any of these formats. There is a structure for each line which contains the molecular data such as oscillator strength and vacuum rest wavelength as well as the calculated data from the fit such as redshift and density. Information on whether the fit for the line converged is also in the structure.

4. Analysis of the H₂ Lines

The purpose of this analysis is to determine as accurately as possible the true vacuum wavelength of the observed H₂ absorption lines in the spectra of Q0347-383 and Q0405-443 produced by the procedures discussed in § 3 and Thompson et al. (2009). These wavelengths are then used in § 5 to measure the value of μ at the epoch represented by the redshift of the DLA absorption line system. The procedures described in the following are procedures written in IDL.

4.1. Establishing the Continuum

Our definition of the continuum in this section is not the true continuum of the quasar spectrum but rather the true spectrum without the H₂ absorption lines. This is the canvas that the H₂ spectrum is painted on. In an analogy to preparing a canvas by sizing it we refer to this as sizing the continuum. The procedure starts with a first guess of the column densities of the first 5 rotational levels of the H₂ electronic and vibrational ground state and calculates the expected line width, defined as all regions less than 90% of the continuum, using a Voigt function, the oscillator strength of the transition, a temperature of 350K and the redshift of the H₂ absorption line system. The kinetic temperature of 350K is equivalent to Doppler parameter of 1.7 km s⁻¹. Initially the redshift was taken from previous studies but subsequent iterations used the best redshift from the previous iteration. There is only one velocity component for Q0347-383 and only the strongest component of the two velocity components in Q0405-443 was used. The natural line shape is convolved with the UVES instrumental profile to produce the observed line profile. This procedure simply defines the spectral region that must be replaced with the continuum estimate. The spectral region inside the line width is then replaced with the expected continuum calculated by interpolating the spectrum on either side of the line which has undergone a 5 pixel smoothing. It is important to note that as mentioned at the beginning of the section this is a local continuum fit which represents what the spectrum would be if there were no molecular hydrogen lines, not the true continuum flux. Since the fit is local there is an independent continuum fit for each line. The typical line spans two to three pixels. The automated continuum calculation gives a rough, first order fit to the sized continuum. At this point a hard copy plot of the spectrum and continuum is produced and examined.

The continuum fit of the selected lines is then interactively refined in an IDL based procedure that displays the fit for each line and allows the user to adjust the fit interactively. The complex spectrum of the Lyman Alpha forest insures that most of the continuum fits must be adjusted. Since the goal of this study is the most precise possible wavelength fit, rather than a column density fit, the continuum is usually adjusted preferentially to lower values that emphasize the line center as opposed to the lower signal to noise wings of the line. Tests with various continuum fits indicated that adjustment of the continuum to higher levels produced significant errors in wavelength for some lines but that adjustment to a reasonable range lower levels did not produce wavelength changes larger than the wavelength errors determined in § 5.2.3. Apparently the larger number of pixels in the high continuum cases allowed noise in the wings of the line to have a greater influence on the fit than with the low continuum case. The line shape convolved with the instrumental profile is about twice as wide as the natural line shape for unsaturated lines. A mosaic of the spectral regions of all of the lines used in the analysis along with the continuum and line fits are shown in

Figures 1 and 2. These spectra are displayed to allow the reader to judge the quality of the continuum and line fits. The spectra at this point are ready for the $\Delta\mu/\mu$ determination.

5. Determination of the $\Delta\mu/\mu$ Value

5.1. Selection of Suitable H_2 Lines for the Measurement of μ

Most of the H_2 lines are unusable due to the Lyman Alpha forest. Appropriate lines are picked at this time based on freedom from interference by other lines and signal to noise. A basic selection rule is lines that have greater than 50% asymmetry between the height of their short wavelength and long wavelength shoulders are rejected. This limits the number of lines used that lie on the shoulders of other lines. Lines that have asymmetric profiles, indicating a blend of two lines, are also rejected. Lines that have profiles broader by 50% than expected from a single line are similarly rejected. Finally lines that do not converge to a stable redshift value in the following analysis are not used to determine the μ value. During the course of the analysis slightly different selection rules were applied. More lenient rules led to larger errors as did more stringent rules that reduced the number of lines in the analysis. In no case, however, did the results exceed a 2σ excursion from a null result. The lists of lines used in this analysis are given in Tables 4 and 5. These line lists do not directly correspond to the lines used by Reinhold et al. (2006) who did not publish their selection criteria but were guided by lines selected by Ivanchik et al. (2005). King et al. (2009) do not list the lines that they used but the text indicates that they were not the same as those use by Reinhold et al. (2006). They did, however, conduct an analysis using the same lines as Reinhold et al. (2006) and obtained a result of $\Delta\mu/\mu = (12.0 \pm 14.0) \times 10^{-6}$. As in the analysis of Reinhold et al. (2006) only the stronger of the double system of H_2 lines in Q0405-443 were used. The two systems are separated by 13 km/sec which is a separation of roughly 4 of the double binned pixels.

5.2. Fitting the Lines

The line fitting procedures are IDL based double precision procedures written and developed by authors. Each line is fit individually rather than calculating a complete synthetic spectrum for several reasons. The first is that most of the large number of molecular hydrogen lines are unusable due to blends with other lines or due to complete obliteration by the Lyman α forest. They would simply contribute noise to the fit. Second we are looking for shifts away from the expected wavelengths that a global fit would wash out. Finally we

allow the column density to be an independent parameter for each line and use anomalous densities to find lines that are blended with other lines.

The individual selected H₂ lines are fit iteratively with alternate adjustments of the wavelength and the column density. The fit function is a Voigt function calculated with the IDL function *VOIGT* that is convolved with the instrument profile. The IDL *VOIGT* function is calculated with double precision parameters and returns a double precision result. The instrument profile is represented by a Gaussian of halfwidth 0.037014 Å at 3900 Å digitized in units of 0.001 Å (Carswell, R. 2005). The halfwidth is adjusted at other wavelengths to be directly proportional to the wavelength. Changes in the width of the Gaussian by plus or minus 10% changed the derived column density but had no effect on the derived wavelength within the wavelength errors attributable to signal to noise. The kinetic and excitation temperature of the gas is not varied but held at 350K for both objects for the initial fitting. During the iteration of the fits we did not require all lines with the same lower state to have the same column density. This is similar to letting the excitation temperature vary from line to line. The kinetic temperature is held fixed at 350K. Changes in the kinetic temperature by ± 100 K did not alter the derived wavelengths within the 1σ bounds.

The fit is started with an initial guess at the column density for each ground state rotational level and an initial guess at the redshift. After a few runs these initial guesses were refined to produce a better starting solution. The fit procedure starts with the wavelength adjustment followed by a column density adjustment. This procedure is iterated 6 times. Lines that have not converged after six iterations are then rerun with another 6 tries at convergence. Any lines that have not converged in both column density and wavelength after the two iterations are not used in the analysis. Convergence is declared when two tries in sequence return the same column density and wavelength values.

5.2.1. Wavelength Iteration

The first of the 6 tries in each iteration starts with a sweep of the wavelength in 200×10^{-5} Å steps on either side of the starting wavelength. The starting wavelength is either the wavelength from the initial guess at the redshift for the first iteration or the best wavelength from the previous try in the second and subsequent iterations. At each of the 200 wavelengths on either side of the initial wavelength the line fit is calculated as a Voigt function superimposed upon the continuum spectrum as discussed in § 4.1 and § 5.2. The calculated spectrum is then convolved with the instrument profile as described in § 5.2. A χ^2 value for the difference between the fit and the observed flux is then calculated for all spectral points in the line that are deeper than 95% of the continuum. After the sweep over the 400

wavelength positions the best wavelength is taken to be the wavelength with the minimum χ^2 value. If the best wavelength is not at either extremum of the wavelength sweep the number of test wavelengths is reduced by a percentage that is proportional to the distance of the best wavelength from the extremum. The minimum number of test wavelengths is 10. Subsequent tries at the wavelength fit are all centered at the best wavelength from the previous try.

5.2.2. *Column Density Iteration*

After each try at the wavelength fit there is an adjustment of the column density. The wavelength is fixed at the best wavelength from the last wavelength iteration. The column density is varied over 200 values ranging from 1% of the initial density to twice the initial density in 1% increments. The initial column density is either the initial guess column density or the density found in previous column density iteration. A χ^2 value is then calculated for all column density points in the same way as the wavelength iteration. The best column density is taken as the density with the minimum χ^2 value. Although the column density range is asymmetric between the high and low ends it usually converges in the first 2 to 3 iterations.

5.2.3. *The χ^2 Values*

Mosaic plots of the χ^2 values calculated for each line are shown in Figures 3 and 4. The values are shown for 100 wavelengths on either side of the best wavelength. The wavelength values are spaced by 10^{-4} Å rather than the 10^{-5} Å spacing in the actual analysis. Note that the χ^2 values are smoothly varying in a semi-parabolic shape with a definite minimum. Murphy, Webb & Flambaum (2008) point out that this is a necessary criterion for valid χ^2 values. Although the values are generally symmetric about the minimum there is significant asymmetry in some of the plots. This is expected from line profiles that are also not symmetric. Only the wavelength, which is the primary parameter of interest, is varied in the plots, as opposed to both the wavelength and the column density in the fitting procedure, so that the minimum χ^2 value is for one degree of freedom. The χ^2 values range from values almost as low as 1.1 to values as high as 45.6, with Q0347-383 having in general lower χ^2 values than Q0405-443 which has a lower signal to noise spectrum. There does not appear to be any correlation between the individual χ^2 values and the deviation of the reduced redshift from the average reduced redshift for each object. The lines with the highest deviation from the average reduced redshift are not the ones with the highest χ^2 values.

The error bars for each line in Figures 5 and 6 are calculated by running the line fit calculations on either side of the minimum χ^2 wavelength until the χ^2 value increases by unity over the minimum χ^2 value. This produces in some cases a significant difference between the positive and negative error bars. The positive and negative errors along with the χ^2 values for the individual line fits are listed in Tables 4 and 5.

5.3. Results

Tables 4 and 5 give the results of the line fitting for Q0347-383 and Q0405-443 respectively. Note that some transitions are repeated since they appear in two different orders. In our analysis we treat these as independent measures. Figures 5 and 6 are the plots of reduced redshift ζ versus sensitivity factor K_i for Q0347-383 and Q0405-443 in manner similar to that first used by Varshalovich & Levshakov (1993). Reinhold et al. (2006) and Ubachs et al. (2007) both display their results with similar plots. The reduced redshift ζ is defined by

$$\zeta_i = \frac{z_i - z_Q}{1 + z_Q} = \frac{\Delta\mu}{\mu} K_i \quad (2)$$

where z_Q is the true redshift of the system taken as the median redshift of all of the lines, z_i is the redshift of individual lines and K_i is defined in Equation 1. The median redshifts of the H₂ absorptions in Q0347-383 and Q0405-443 are 3.0248996 and 2.5947366 respectively, relative to the earth - sun barycenter. The slope in this plot is the value of $\Delta\mu/\mu$.

The thick black dash dot and dash triple dot lines in the figures are the weighted and unweighted linear least squares fits to the combined data for all rotational levels for each object where the weights are determined by the standard deviations of the individual data points. The colored light solid and dotted lines are the fits to only lines with the same rotational level ground states given by the color codes in the caption. The weighted and unweighted fits to Q0347-383 are $\Delta\mu/\mu = (-28 \pm 16) \times 10^{-6}$ and $\Delta\mu/\mu = (-19 \pm 15) \times 10^{-6}$. The weighted and unweighted fits for Q0405-443 are $\Delta\mu/\mu = (0.55 \pm 10) \times 10^{-6}$ and $\Delta\mu/\mu = (3.7 \pm 14) \times 10^{-6}$. For the combined data set shown in Figure 7 the weighted fit yields $\Delta\mu/\mu = (-7.0 \pm 8) \times 10^{-6}$ and the unweighted fit gives $\Delta\mu/\mu = (-6 \pm 10) \times 10^{-6}$. Both of these results are consistent with no variation in μ at the 68% confidence level. Our result is consistent with the findings of Wendt and Reimers (2008) giving $-7.0 \times 10^{-6} \leq \Delta\mu/\mu \leq 49 \times 10^{-6}$ and King et al. (2009) which give $\Delta\mu/\mu = (2.6 \pm 3.0) \times 10^{-6}$. They are inconsistent at a roughly 3σ level with that of Reinhold et al. (2006) and Ubachs et al. (2007) who found $\Delta\mu/\mu = (24.5 \pm 5.9) \times 10^{-6}$.

The stated errors between the three measurement vary widely. It should be noted that the error quoted by Wendt and Reimers (2008) is a 2σ error so the value $\pm 25 \times 10^{-6}$ should be used in comparison to the other two measurements. King et al. (2009) perform an analysis where they use the same lines as Ubachs et al. (2007) and their error grows to about $\pm 9 \times 10^{-6}$ for the individual objects. This error is similar but slightly smaller than our errors. King et al. (2009) also include a third object Q0528-250 which has a significantly smaller quoted error than the two objects common to all of the studies. In the weighted mean of errors Q0528-250 has a dominant effect on the quoted error. In the following we discuss our error analysis.

5.4. Error Analysis

The least squares linear fit to the weighted combined data of 77 lines gives a χ^2 value of 104.9. Assuming N-2 degrees of freedom this is a χ^2 value of 1.4 per degree of freedom. In the combined data there are 10 pairs of lines of the same transition but observed in a different orders. Q0347-383 has 4 pairs and Q0405-443 has 6 pairs. We have treated these as independent measurements since they have independent photon noise and read noise statistics. Systematic effects such as unknown blended lines and continuum shape may introduce systematics into the measurements. Individual inspection of the line pairs indicates that the dispersion in reduced redshift between the two measurements is consistent with the dispersion between independent lines and should not bias the results.

5.4.1. Bootstrap Analysis

As an alternative check on the statistical significance of the null result we performed a bootstrap analysis on the combined data set. We produced 10,000 new data sets by drawing the same number of lines but randomly selected allowing duplication from the original data set. Linear least square fits were performed on the data sets and the result plotted as a histogram shown in Figure 8. The smooth curve in the figure is a Gaussian fit to the histogram. The peak of the Gaussian is at a $\Delta\mu/\mu$ value of -6.4×10^{-6} and the half width at half maximum is 12×10^{-6} , both of which are consistent with the results of the χ^2 analysis. The histogram values conform to the Gaussian fit quite well indicating the appropriateness of the assumption of Gaussian distributed errors.

5.4.2. *Ground State Rotational Levels*

Since transitions from 4 different rotational levels ($J=0,1,2,3$) are used it is possible that the transitions could arise from physically offset regions of the molecular cloud that could also have velocity offsets. Our null result is less prone to this type of error, however, velocity offsets could be in a direction to reduce a $\Delta\mu/\mu$ signal. To check for this the solutions for lines with the same rotational ground level and the same object are plotted in Figures 5 and 6. In Q0347-383 there is only one line with a ground rotational level of 0 so no solution is plotted for it. The $J=1$ and 3 solutions have roughly the same slope while the $J=2$ solution has a different slope with the opposite sign. This would appear difficult to achieve with physical velocity offsets which would be presumed to have a smooth gradient of velocity with temperature. In Q0405-443 there are no $J=0$ lines and only one $J=1$ line so no solutions exist for those systems. The $J=2$ and $J=3$ slopes are of opposite sign but within the error bars of each other. From this analysis we conclude that it is unlikely that velocity gradients with excitation level are masking a change in μ .

5.4.3. *Combination of the Data Sets*

To improve the statistics of the sample we have combined the lines from the two systems. The higher redshift system associated with Q0347-383 shows a shift in μ at the 1σ level in the unweighted fit and at a 1.75σ level in the weighted fit, both indicating a decrease in the value of μ . The system associated with Q0405-443 at a lower redshift shows an increase in μ in both the unweighted and weighted fit but at levels significantly less than 1σ . The Q0405-443 system has 7 more lines than the Q0347-383 system. It could be argued that the combination of the two data sets dilutes the signal of a real shift in the Q0347-383 system at the higher redshift and earlier time in the universe. Although we would not claim a real shift in μ with a 1.75σ result we can not rule out that the combined data set is diluting the evidence for a change in μ . The higher than expected value of the χ^2 per degree of freedom could be due to the difference in fitted slopes of the two systems taken separately.

5.4.4. *Systematics*

The method of sensitivity coefficient fitting is subject to systematic errors in the wavelength scale. In general the sensitivity coefficients increase with increasing vibrational energies in the upper level of the transitions. This means that for a given electronic transition system the sensitivity coefficient increases with decreasing transition wavelength. That

means that any systematic error that produces an erroneous gradient in the wavelength calibration will mimic a change in μ . This is mitigated to some degree by the mixture of Lyman and Werner bands. The higher electronic energy of the upper level of the Werner system places low values of the sensitivity coefficient at the same wavelengths as high sensitivity coefficient Lyman transitions. At wavelengths longer than the longest wavelengths of the Werner system, however, there is no mitigating effect. It may be this effect coupled with the systematic errors in the older UVES pipeline reductions found by Murphy et al. (2008a) that produced the positive detection of a change in μ by Reinhold et al. (2006). The analysis in Thompson et al. (2009), Figures 7 and 8, indicates that the wavelength calibration used in this analysis is not subject to systematic errors of the magnitude cited in Murphy et al. (2008a). In addition our wavelength calibration is on an order by order basis which resets the solution for each order, making it more difficult to have systematic effects over the whole wavelength solution.

5.4.5. *Comparison of Lyman and Werner Lines*

The Werner lines with a higher upper electronic level provide lines with low upper state vibrational levels at wavelengths that are close to Lyman lines with high upper state vibrational levels. Since the sensitivity factors are roughly proportional to upper state vibrational level this mixes lines with low sensitivity factors with those with high factors. Under the assumption that any possible systematic wavelength errors are minimized for lines that lie close together we have looked at the redshift differences between all of the Werner lines and the Lyman lines that are adjacent to them in the same order. There are a limited number of line pairs that satisfy this criterion, 8 for Q0347-383 and 7 for Q0405-443. Histograms of the distribution are given in Figure 9. The distribution of delta redshift values ($z(\text{Lyman}) - z(\text{Werner})$) for Q0405-443 are roughly evenly distributed around zero but the delta redshift values for Q0347-383 are all negative. This is consistent with the negative slope of the fit in Figure 5.

5.5. **The Marginal Possibility of a Shift in Q0347-383**

The analysis results for Q0347-383 show a negative shift in the value of μ at the 1.75 σ level which has a statistical probability of being a true shift at the 91% percent level if the errors are Gaussian distributed. This is certainly not a level which justifies declaring a change in a fundamental constant but raises the marginal possibility that there might be a change. In addition the comparison between the Werner and Lyman lines in Figure 9

shows a negative delta between the Werner and Lyman lines for a seven cases which has a probability of $2^{-7} = 0.008$ chance of happening randomly. If a monotonically rolling scalar field is invoked for the change, the higher redshift of Q0347-383 could be why a change is seen in Q0347-383 and not Q0405-443. We consider this evidence as suggestive but in no way conclusive. It does point out the need for observations of systems at higher redshift.

6. Conclusions and Implications

Our basic conclusion, based on the combination of data from Q0347-383 and Q0405-443, is that there has been no change in the value of μ to 1 part in 10^5 over a time span of 11.5 gigayears. This is approximately 80% of the age of the universe. The accuracy of the limit on $\Delta\mu/\mu$ is set by both the spectral resolution and the signal to noise ratio of the flux. This conclusion is consistent with the results of King et al. (2009) but inconsistent with the results of Reinhold et al. (2006). Starting with the same raw data, the primary difference in this analysis is the use of improved wavelength calibration techniques that eliminated the systematic variations in the calibration used in the UVES pipeline at the time of the Reinhold et al. (2006) analysis. The line selection is also most likely different from Reinhold et al. (2006) but without a list of those lines it is difficult to assess the influence of the lines chosen. There is a marginal possibility of the detection of a change in μ based on the Q0347-383 data alone. We, however, feel that this result while suggestive is certainly not conclusive.

What implications does a limit on $\Delta\mu/\mu$ of 10^{-5} have on theories of dark energy that invoke a rolling scalar field potential as the source of the dark energy? Chongchitnan & Efstathiou (2007) have despaired about distinguishing between a universe with a cosmological constant relative to a universe with a quintessence rolling scalar field, however, the former predicts no change in μ while the latter predicts a change even though the magnitude or even the sign of the change is not presently calculable. Detection of a change in μ or its companion the fine structure constant α would be strong evidence for quintessence as opposed to a cosmological constant.

Quintessence is usually expressed in terms of a potential $V(\phi)$ that is a function of the rolling scalar ϕ . The change in μ is then expressed as

$$\frac{\Delta\mu}{\mu} = \zeta_\mu \kappa (\phi - \phi_0) \quad (3)$$

where κ is $\sqrt{8\pi}/m_{Pl}$, m_{Pl} is the Planck mass and ζ_μ is a parameter of unknown value

(Avelino, Martins, Nunes & Olive (2006) and references therein). Determination of the value of μ at high redshift is therefore a direct way to distinguish between quintessence and a cosmological constant. In Grand Unified Theories (GUTs) the rolling of μ is typically given by

$$\frac{\dot{\mu}}{\mu} \sim \frac{\dot{\Lambda}_{QCD}}{\Lambda_{QCD}} - \frac{\dot{\nu}}{\nu} \sim R \frac{\dot{\alpha}}{\alpha} \quad (4)$$

where Λ_{QCD} is the QCD scale, ν is the Higgs Vacuum Expectation Value (VEV), R is a model dependent value (Avelino, Martins, Nunes & Olive (2006) and references therein) and α is the fine structure constant. In many GUT models the value of R is large and negative ~ -50 (Avelino, Martins, Nunes & Olive (2006)).

Our current results limit the value of $\zeta_{\mu}\kappa(\phi - \phi_0)$ in Equation 3 to be on the order of 10^{-5} or less, but does not tell us the individual values of $(\phi - \phi_0)$ or ζ_{μ} . The results do, however, rule out Model A of Avelino, Martins, Nunes & Olive (2006) at about the 4σ level where the potential is given by

$$V(\phi) = V_0(\exp(10\kappa\phi) + \exp(0.1\kappa\phi)) \quad (5)$$

which predicts a value of $\frac{\Delta\mu}{\mu} = 3 \times 10^{-5}$ at a redshift of 3. This means that even at the current level of accuracy significant bounds on the quintessence models are being established. In all fairness to the model it must be pointed out that it was designed to achieve that result to match the findings of Reinhold et al. (2006).

If the claim of a detected change in the fine structure constant α ($\frac{\Delta\alpha}{\alpha} = 0.57 \times 10^{-5}$ (Murphy, Webb & Flambaum (2003))) is accepted then this implies a value of R of ≤ 2 which is significantly different in sign and magnitude that the typical GUT value quoted above. This would mean that either the roll of both the QCD scale and the Higgs VEV is small or that they are equal to each other by less than a factor of 2. Of course if the claim for a change in α is not accepted the current limitation on $\frac{\Delta\mu}{\mu}$ places no limit on R .

RIT would like to acknowledge interesting and useful conversations with Wim Ubachs, Dimitrios Psaltis, Feryal Ozel and Michael Murphy on theory and technique. C.M. wishes to acknowledge very useful discussions with Paolo Molaro. The work of C.M. is funded by a Ciencia2007 research grant.

REFERENCES

- Abgrall, H., Roueff, E., Launay, F., Roncin, J.-Y. & Subtil, J.-L. 1993, A&AS, 101, 273
- Abgrall, H., Roueff, E., Launay, F., Roncin, J.-Y. & Subtil, J.-L. 1993, A&AS, 101, 323
- Avelino, P.P., Martins, C.J.A.P., Nunes, N.J., & Olive, K.A. 2006, Phys. Rev. D, 74, 083508
- Barrow, J. D., Sandvik, H. B., & Magueijo, J. 2002, Phys. Rev.D, 65, 63504
- Blatt, S. et al. 2008, PRL, 100, 140801
- Carswell R., Private communication.
- Chongchitnan, S. & Efstathiou, G. 2007, Phys. Rev. D., 76, 043508.
- Cowie, L.L. & Songaila, A. 1995 ApJ, 453, 596
- Damour, T. & Dyson, F. J. 1996 Nucl. Phys. B, 480, 37
- Dekker, H., D’Odorico, S., Kaufer, A., Delabre, B. & Kotzlowski, H. 2000, Proc. SPIE Optical and IR Telescope Instrumentation and Detectors, I. Masanori & A.F. Moorwood ed., 4008, 534
- Dent, T., Stern, S., & Wetterich, C. 2008, arXiv:0812.4130v1
- Dirac, P.A.M. 1937, Nature, 139, 323
- D’Odorico, S., Dessauges-Zavadsky, M., & Molaro, P. 2001, A&A, 368, L21
- Flambaum, V.V. & Kozlov, M.G. 2007, Phys. Rev. Lett., 98, 240801
- Foltz, C. B., Chaffee, F.H., & Black, J.H. 1988, ApJ, 324, 267
- Gamow, G. 1967, Phys. Rev. Lett., 19, 759
- Ivanchik, A.V. et al. 2002, Astronomy Letters, 28, 423 (page 483 in *Astronomicheskii Zhurnal*)
- Ivanchik, A., Petitjean, P., Rodriguez, E. & Varshalovich, D. 2003, Ap&SS, 283, 583
- Ivanchik, A. et al. 2005, A&A, 440, 45
- Ivanov, T.I., Vieitez, M.O., de Lange, C.A. & Ubachs, W. 2008, J. Phys. B: At. Mol. Opt. Phys. 41, 035702

- King, J. A., Webb, J. K., Murphy, M. T. & Carswell, R. F. 2009, Phys. Rev. Lett., 101, 251304
- Levshakov, S. A. et al. 2002, MNRAS, 333, 373.
- Levshakov, S. A., Molaro, P. & Kozlov, M. G. 2008 astro-ph0808.0583v1
- Murphy, M.T., Webb, J.K., & Flambaum, V.V. 2003, MNRAS, 345, 609
- Murphy, M.T., Webb, J.K., & Flambaum, V.V. 2008, MNRAS, 384, 1053
- Murphy, M.T., Tzanavaris, P., Webb, J.K. & Lovis, C. 2008, MNRAS, 378, 221
- Murphy, M.T., Flambaum, V.V., Muller, S., Henkel, C. 2008, Science, 320, 1611
- Philip, J. et al. 2004, Can. J. Chem, 82, 713
- Potekhin, A.Y. et al. 1998, ApJ, 505, 523
- Shelkovnikov, A., Butcher, R.J., Chardonnet, C., Amy-Klein, A. 2008 PRL, 100, 150801
- Reinhold, E. et al. 2006, Phys. Rev. Lett., 96, 151101
- Shu, F.H. The Physics of Astrophysics Volume I Radiation, Mill Valley: University Science Books 1991
- Teller, E. 1948, Phys. Rev., 73, 801
- Thompson, R.I. 1975 Astrophysical Letters, 16, 3
- Thompson, R. I., Bechtold, J, Black, J. H. & Martins, C. 2009, New Astronomy, 14, 379
- Ubachs, W. & Reinhold 2004, Phys. Rev. Lett., 92, 101302
- Ubachs, W., Buning, R., Eikema, K. S. E. & Reinhold, E. 2007, Jour. Mol. Spec., 241, 155
- Uzan, J-P 2003, Rev. Mod. Phys., 75, 403
- Varshalovich, D. & Levshakov, S. 1993, JETP Letters, 58, 231
- Vogt, S.S. et al. 1994, Proc. SPIE Instrumentation in Astronomy VIII, D.L. Crawford & E.R. Craine ed., 2198, 362
- Wendt, M. & Reimers, D. 2008, Eur. Phys. J. ST, 163, 197
- Wolfe, A.M., Gawiser, E. & Prochaska, J.X. 2005, ARA&A, 43, 861

Table 1. Recent Astronomical μ Measurements

Object	Reference	Redshift	$\Delta\mu/\mu$
PKS 0528-250	Foltz, Chaffee & Black (1988)	2.811	$ \leq 2 \times 10^{-4}$
PKS 0528-250	Cowie & Songaila (1995)	2.811	$ \leq 7 \times 10^{-4}$
PKS 0528-250	Potekhin et al. (1998)	2.811	$ \leq 2 \times 10^{-4}$
Q0347-383 + Q1232+082	Ivanchik et al. (2002)	3.0249	$(5.7 \pm 3.8) \times 10^{-5}$
Q0347-383	Levshakov et al. (2002)	3.0249	$-1.5 \times 10^{-5} \leq 5.7 \times 10^{-5}$
Q0347-383	Ivanchik et al. (2003)	3.0249	$ \leq 8 \times 10^{-5}$
Q0347-383	Wendt and Reimers (2008)	3.0249	$-0.7 \times 10^{-5} \leq 4.9 \times 10^{-5}$
Q0347-383 + Q0405-443	Ubachs & Reinhold (2004)	3.0249, 2.5974	$(-0.5 \pm 3.8) \times 10^{-5}$
Q0347-383 + Q0405-443	Ivanchik et al. (2005)	3.0249, 2.5974	$(1.64 \pm 0.74) \times 10^{-5}$
Q0347-383 + Q0405-443	Reinhold et al. (2006)	3.0249, 2.5974	$(2.4 \pm 0.6) \times 10^{-5}$
Q0347-383 + Q0405-443	Reinhold et al. (2006)	3.0249, 2.5974	$(2.45 \pm 0.59) \times 10^{-5}$
Q0347-383 + Q0405-443	this work	3.0249, 2.5974	$(-7 \pm 8) \times 10^{-6}$
Q0347-383 + Q0405-443 + PKS 0528-250	King et al. (2009)	3.0249, 2.5974, 2.811	$(2.6 \pm 3.0) \times 10^{-6}$
B0218+357	Flambaum & Kozlov (2007)	0.6847	$(0.6 \pm 1.9) \times 10^{-6}$
B0218+357	Murphy et al. (2008b)	0.6847	$ \leq 0.18 \times 10^{-6}$
Milky Way	Levshakov, Molaro & Kozlov (2008)	0.0	$(4 - 14) \times 10^{-8}$

Table 2. Observational Parameters for Q0347-383

Archive File	Date	Seconds Exp.
UVES_2002_01_08T00:46:05_351_b.fits	8 Jan. 2002	4500
UVES_2002_01_08T02:03:41_018_b.fits	8 Jan. 2002	4500
UVES_2002_01_08T03:21:18_348_b.fits	8 Jan. 2002	4500
UVES_2002_01_09T00:43:43_109_b.fits	9 Jan. 2002	4500
UVES_2002_01_09T02:02:11_833_b.fits	9 Jan. 2002	4500
UVES_2002_01_09T03:19:58_841_b.fits	9 Jan. 2002	4500
UVES_2002_01_10T00:48:56_171_b.fits	10 Jan. 2002	4500
UVES_2002_01_10T02:06:28_725_b.fits	10 Jan. 2002	4500
UVES_2002_01_10T03:24:33_981_b.fits	10 Jan. 2002	4500

Table 3. Observational Parameters for Q0405-443

Archive File	Date	Exposure Time
UVES_2003_01_04T00:43:06_274_b.fits	4 Jan. 2003	4500
UVES_2003_01_04T02:09:06_464_b.fits	4 Jan. 2003	4500
UVES_2003_01_04T03:34:08_623_b.fits	4 Jan. 2003	4500
UVES_2003_01_05T00:48:35_827_b.fits	5 Jan. 2003	4500
UVES_2003_01_05T02:16:14_922_b.fits	5 Jan. 2003	4500
UVES_2003_01_05T03:46:36_522_b.fits	5 Jan. 2003	4500
UVES_2003_01_06T00:45:18_207_b.fits	6 Jan. 2003	4500
UVES_2003_01_06T02:15:26_790_b.fits	6 Jan. 2003	4500
UVES_2003_01_06T03:46:49_242_b.fits	6 Jan. 2003	4500

Table 4. Q0347-383 Line List

Trans. ^a	order	K factor	Obs. wavelength ^b	pos. error	neg. error	χ^2	Rest wavelength ^b	redshift ^c
L15P1	123	0.05147000	3782.21819	0.0112	-0.0094	3.56	939.70672	3.02489213
L14R1	123	0.04625000	3811.49618	0.0069	-0.0089	7.84	946.98040	3.02489448
W3Q1	123	0.02149000	3813.28002	0.0110	-0.0062	2.73	947.42188	3.02490179
W3Q1	122	0.02149000	3813.28420	0.0079	-0.0055	3.59	947.42188	3.02490620
W3P3	122	0.02097000	3830.37745	0.0056	-0.0049	6.23	951.67186	3.02489304
L13R1	121	0.04821000	3844.04623	0.0046	-0.0043	11.31	955.06582	3.02490189
L13P1	121	0.04772000	3846.62792	0.0085	-0.0076	6.33	955.70827	3.02489760
W2Q1	120	0.01396000	3888.44675	0.0052	-0.0058	30.09	966.09608	3.02490687
W2Q2	120	0.01272000	3893.21423	0.0097	-0.0078	8.29	967.28110	3.02490468
L12R3	120	0.03682000	3894.80256	0.0085	-0.0088	1.16	967.67695	3.02489959
W2Q3	120	0.01088000	3900.33218	0.0042	-0.0040	15.21	969.04922	3.02490617
W1Q1	118	0.00487000	3971.76790	0.0037	-0.0054	3.82	986.79800	3.02490469
W1Q1	117	0.00487000	3971.76771	0.0075	-0.0130	2.04	986.79800	3.02490450
L9R1	117	0.03753000	3992.75767	0.0034	-0.0038	8.86	992.01637	3.02489091
L8R0	116	0.03475000	4032.24698	0.0066	-0.0075	6.32	1001.82387	3.02490607
L8R1	116	0.03408000	4034.76532	0.0051	-0.0041	16.47	1002.45210	3.02489587
L8R1	115	0.03408000	4034.75032	0.0104	-0.0097	10.49	1002.45210	3.02488091
W0R2	115	-0.00525000	4061.22312	0.0083	-0.0104	11.53	1009.02492	3.02489873
W0Q2	115	-0.00710000	4068.92599	0.0067	-0.0070	27.08	1010.93845	3.02489982
W0Q2	114	-0.00710000	4068.91220	0.0138	-0.0157	4.71	1010.93845	3.02488618
L7R1	114	0.03027000	4078.98076	0.0063	-0.0093	7.84	1013.43701	3.02489816
L7P3	114	0.02460000	4103.38732	0.0046	-0.0053	2.64	1019.50224	3.02489289
L6P3	112	0.02033000	4150.43809	0.0083	-0.0182	2.55	1031.19260	3.02489126
L5P1	112	0.02064000	4178.48451	0.0086	-0.0089	12.21	1038.15713	3.02490566
L5R2	112	0.01997000	4180.62771	0.0074	-0.0064	4.82	1038.69027	3.02490313
L4P2	110	0.01346000	4239.36224	0.0061	-0.0046	2.54	1053.28426	3.02489850
L4P3	110	0.01051000	4252.19544	0.0070	-0.0065	4.61	1056.47144	3.02490335
L3R1	109	0.01099000	4280.32103	0.0042	-0.0042	45.60	1063.46014	3.02490030
L3P1	109	0.01001000	4284.92877	0.0059	-0.0058	8.87	1064.60539	3.02489862
L3R2	109	0.00953000	4286.49249	0.0073	-0.0073	12.69	1064.99481	3.02489519
L3R3	109	0.00719000	4296.48519	0.0041	-0.0042	9.06	1067.47855	3.02489136
L2P2	107	0.00184000	4351.98530	0.0113	-0.0135	8.78	1081.26603	3.02489783
L2P3	107	-0.00115000	4365.24899	0.0138	-0.0117	18.47	1084.56034	3.02490192
L1R1	106	-0.00143000	4398.14064	0.0054	-0.0052	22.80	1092.73243	3.02490172
L1P1	106	-0.00259000	4403.45255	0.0038	-0.0036	22.80	1094.05198	3.02490250

^aTransitions are labeled with L or W for Lyman or Werner, then the vibrational quantum number of the upper state, next R, Q or P transitions and finally the rotational quantum number of the lower state

^bVacuum wavelength

^cBarycentric redshift

Table 5. Q0405-443 Line List

Trans. ^a	order	K factor	Obs. wavelength ^b	pos. error	neg. error	χ^2	Rest wavelength ^b	redshift ^c
L16P1	139	0.05297000	3351.25678	0.0040	-0.0066	5.30	932.26621	2.59474230
W4P2	139	0.02569000	3352.45726	0.0052	-0.0066	2.66	932.60468	2.59472489
W4P3	139	0.02350000	3360.32455	0.0060	-0.0072	1.27	934.79006	2.59473715
L15P3	138	0.04676000	3394.61670	0.0083	-0.0058	10.34	944.33046	2.59473389
W3R2	137	0.02287000	3404.62607	0.0037	-0.0041	13.42	947.11169	2.59474612
L14R2	137	0.04715000	3409.50987	0.0049	-0.0043	13.11	948.47125	2.59474246
W3Q3	137	0.01828000	3416.42562	0.0029	-0.0028	5.69	950.39773	2.59473251
L13P2	136	0.04577000	3442.49784	0.0049	-0.0049	14.30	957.65223	2.59472649
L12P2	134	0.04341000	3473.51556	0.0142	-0.0071	6.53	966.27550	2.59474659
W2P3	134	0.00992000	3488.92549	0.0077	-0.0080	28.26	970.56332	2.59474279
L11P2	133	0.04092000	3506.10669	0.0088	-0.0053	3.54	975.34576	2.59473208
L9R2	131	0.03594000	3571.54986	0.0023	-0.0020	7.52	993.55061	2.59473370
L9P2	131	0.03489000	3576.31685	0.0031	-0.0045	9.02	994.87408	2.59474322
L9P2	130	0.03489000	3576.30117	0.0026	-0.0028	18.84	994.87408	2.59472746
L9P3	130	0.03202000	3586.92017	0.0078	-0.0057	8.06	997.82718	2.59473087
L8R2	130	0.03251000	3609.06404	0.0076	-0.0083	6.95	1003.98545	2.59473739
L8R2	129	0.03251000	3609.06183	0.0073	-0.0052	5.13	1003.98545	2.59473519
L8P2	129	0.03137000	3614.13175	0.0037	-0.0038	12.62	1005.39320	2.59474457
W0R3	128	-0.00631000	3631.14901	0.0049	-0.0046	7.27	1010.13025	2.59473346
W0Q2	128	-0.00710000	3634.05522	0.0035	-0.0041	23.82	1010.93845	2.59473440
L7P2	128	0.02750000	3653.90105	0.0045	-0.0044	15.12	1016.46125	2.59472734
L6P2	127	0.02324000	3695.76334	0.0040	-0.0125	21.67	1028.10609	2.59472954
L6P2	126	0.02324000	3695.77191	0.0034	-0.0079	6.73	1028.10609	2.59473788
L5P2	125	0.01857000	3739.84184	0.0039	-0.0037	11.57	1040.36733	2.59473210
L5R3	125	0.01759000	3742.68792	0.0040	-0.0038	17.41	1041.15892	2.59473260
L5P3	125	0.01564000	3751.12621	0.0030	-0.0043	26.05	1043.50319	2.59474340
L5P3	124	0.01564000	3751.12050	0.0031	-0.0031	10.63	1043.50319	2.59473793
L4R2	124	0.01497000	3779.85697	0.0048	-0.0040	15.03	1051.49857	2.59473334
L4R3	123	0.01261000	3788.77180	0.0054	-0.0038	25.20	1053.97610	2.59474166
L3P2	122	0.00790000	3835.21789	0.0037	-0.0040	17.12	1066.90068	2.59472813
L3R3	122	0.00719000	3837.30732	0.0033	-0.0035	10.22	1067.47855	2.59473951
L3P3	122	0.00493000	3846.87296	0.0057	-0.0044	5.16	1070.14088	2.59473508
L3P3	121	0.00493000	3846.87940	0.0040	-0.0054	16.28	1070.14088	2.59474110
L2R2	121	0.00360000	3879.52758	0.0031	-0.0030	8.81	1079.22542	2.59473332
L2R2	120	0.00360000	3879.53298	0.0021	-0.0022	7.05	1079.22542	2.59473832
L1P2	119	-0.00475000	3941.40916	0.0044	-0.0034	20.26	1096.43894	2.59473657
L1R3	119	-0.00509000	3942.44064	0.0034	-0.0042	8.44	1096.72534	2.59473835
L1P2	118	-0.00475000	3941.41164	0.0031	-0.0043	8.44	1096.43894	2.59473884
L1P3	118	-0.00775000	3953.45055	0.0061	-0.0050	8.44	1099.78718	2.59474144
L0R0	117	-0.00800000	3983.42760	0.0040	-0.0090	8.44	1108.12733	2.59473816
L0P2	117	-0.01191000	3999.12069	0.0028	-0.0028	8.44	1112.49600	2.59472815
L0R3	117	-0.01202000	3999.42503	0.0084	-0.0105	8.44	1112.58000	2.59473029

^aTransitions are labeled with L or W for Lyman or Werner then the vibrational quantum number of the upper state, R, Q or P transitions and finally the rotational quantum number of the lower state

^bVacuum wavelength

^cBarycentric redshift

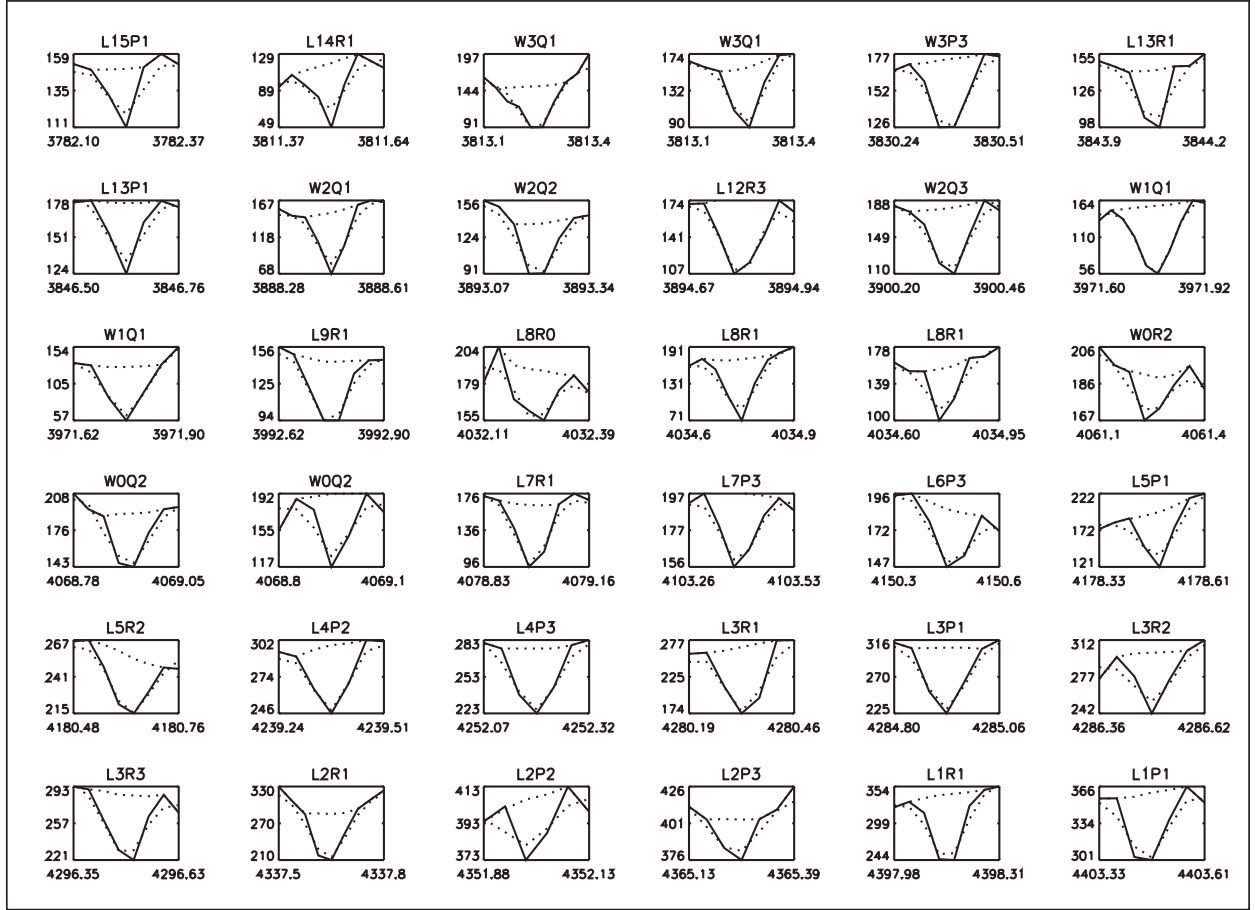


Fig. 1.— The spectrum of Q0347-383 in the regions of the H_2 lines used in this analysis is shown by the solid line. The adopted continuum and fits convolved with the instrument profile are shown by the dotted lines. Repeated transitions are the same H_2 line but in different orders. Transitions are labeled in the same manner as in Tables 4 and 5. The intensities are give in ADUs per second.

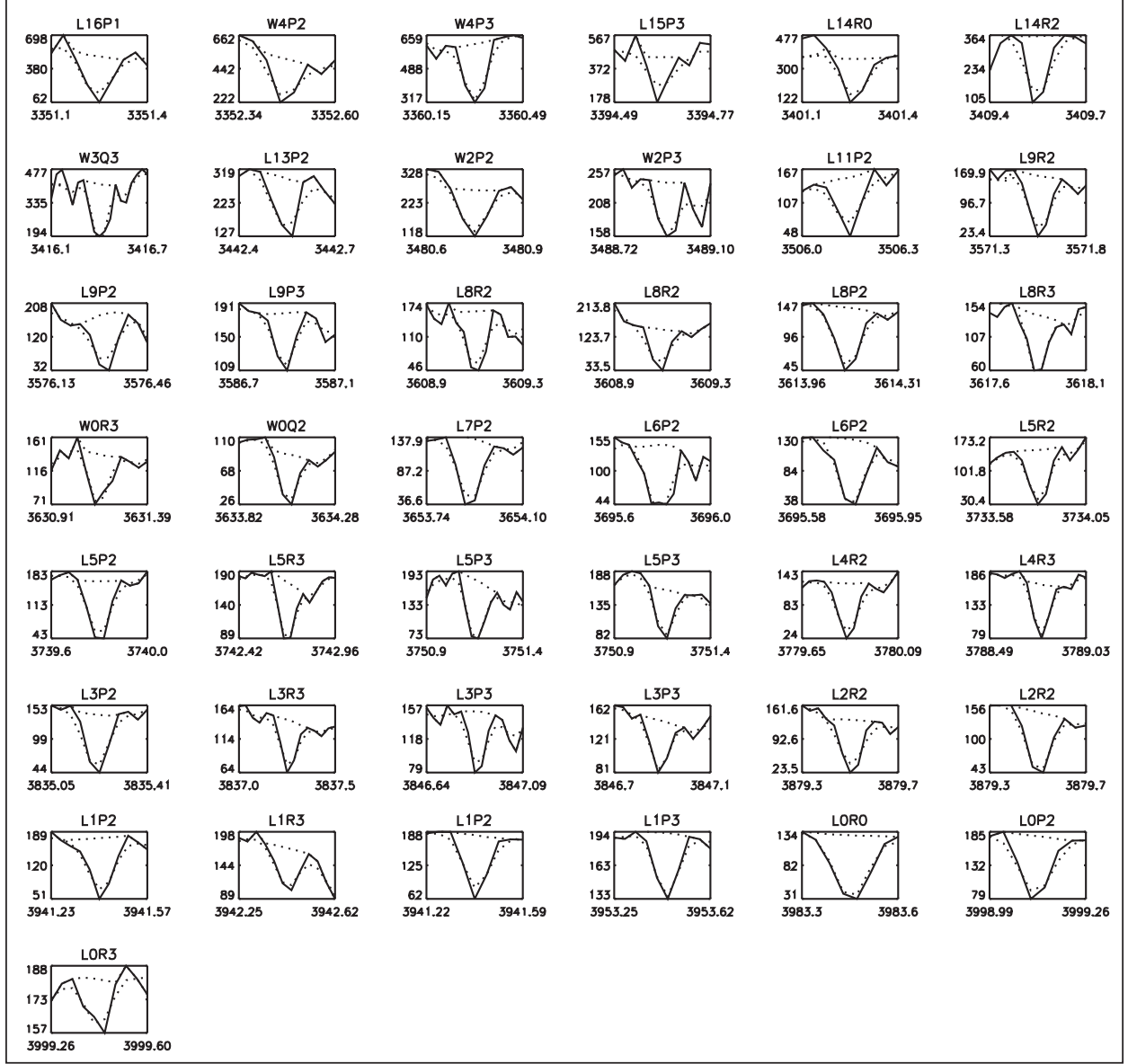


Fig. 2.— The spectrum of Q0405-443 in the regions of the H_2 lines used in this analysis is shown by the solid line. The adopted continuum and fits convolved with the instrument profile are shown by the dotted lines. Repeated transitions are the same H_2 line but in different orders. Transitions are labeled in the same manner as in Tables 4 and 5.

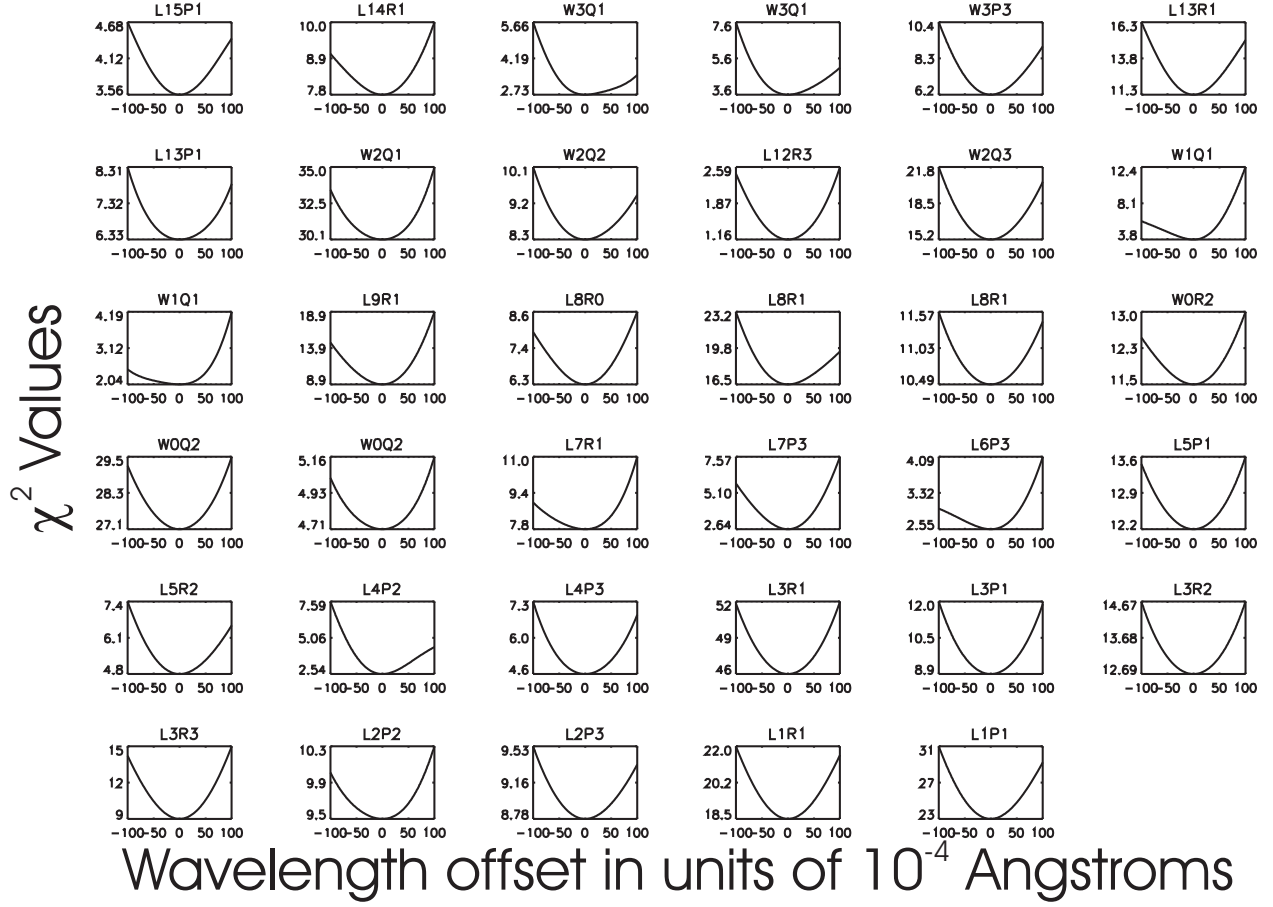


Fig. 3.— The χ^2 values for a sweep of wavelengths in 10^{-4} Å increments around the line wavelength at the minimum χ^2 value for Q0347-383. Note that the actual analysis used wavelength increments of 10^{-5} Å rather than 10^{-4} . Transitions are labeled in the same manner as in Tables 4 and 5.

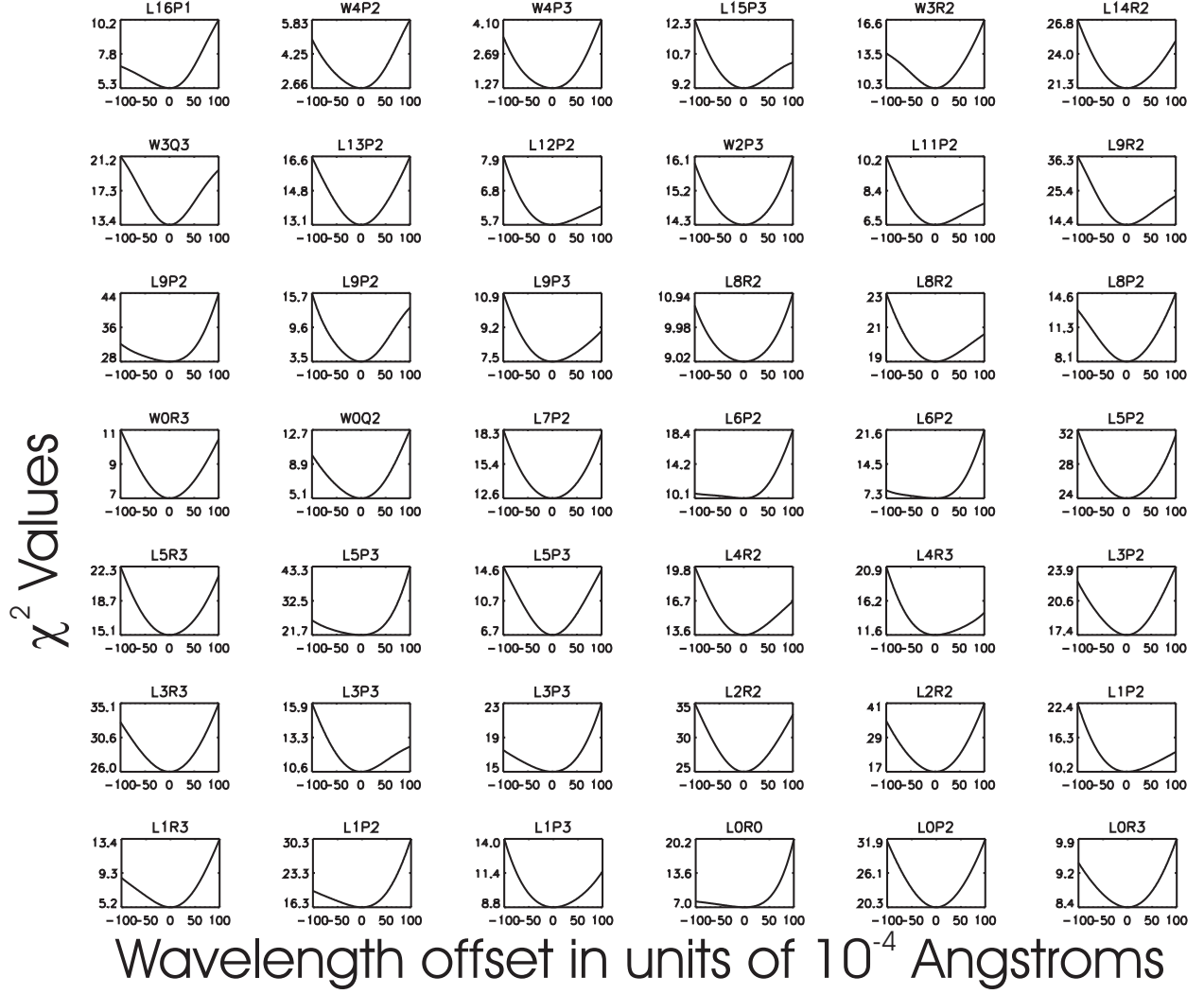


Fig. 4.— The χ^2 values for a sweep of wavelengths in 10^{-4} Å increments around the line wavelength at the minimum χ^2 value for Q0405-443. Note that the actual analysis used wavelength increments of 10^{-5} Å rather than 10^{-4} . Transitions are labeled in the same manner as in Tables 4 and 5.

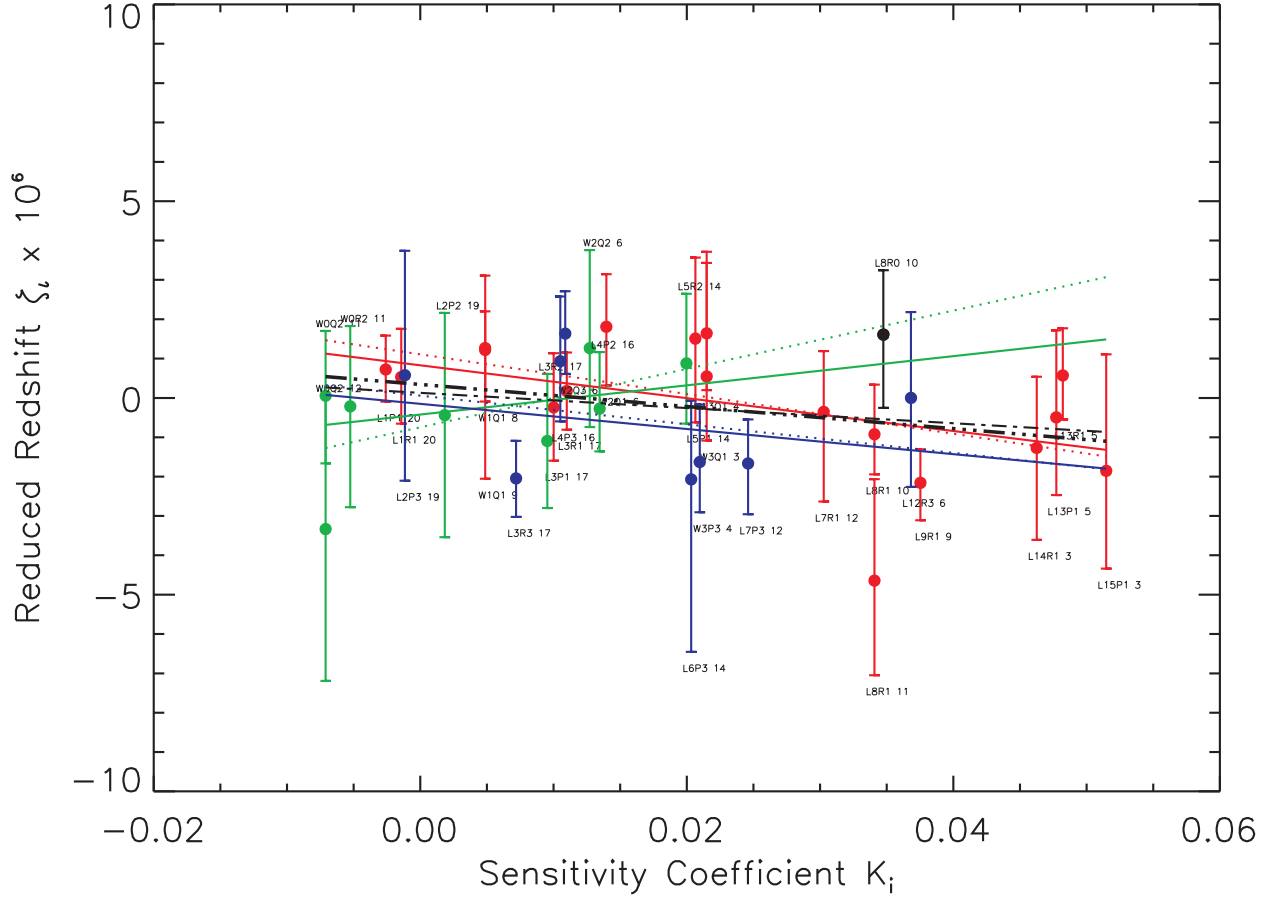


Fig. 5.— The reduced redshift versus sensitivity factor plot for Q0347-383. In the electronic version the symbols are color coded according to the rotational level of the lower electronic state. $J=0$ (black), $J=1$ (red), $J=2$ (green), $J=3$ (blue). The solid line is the weighted fit and the dotted line is the unweighted fit to the individual J levels. The thick dash 3 dot line is the weighted fit and the thick dash dot line the unweighted fit to all J levels combined. The transitions are labeled with the last number being the order. The orders are the observed order with the true order being 126 minus the printed number.

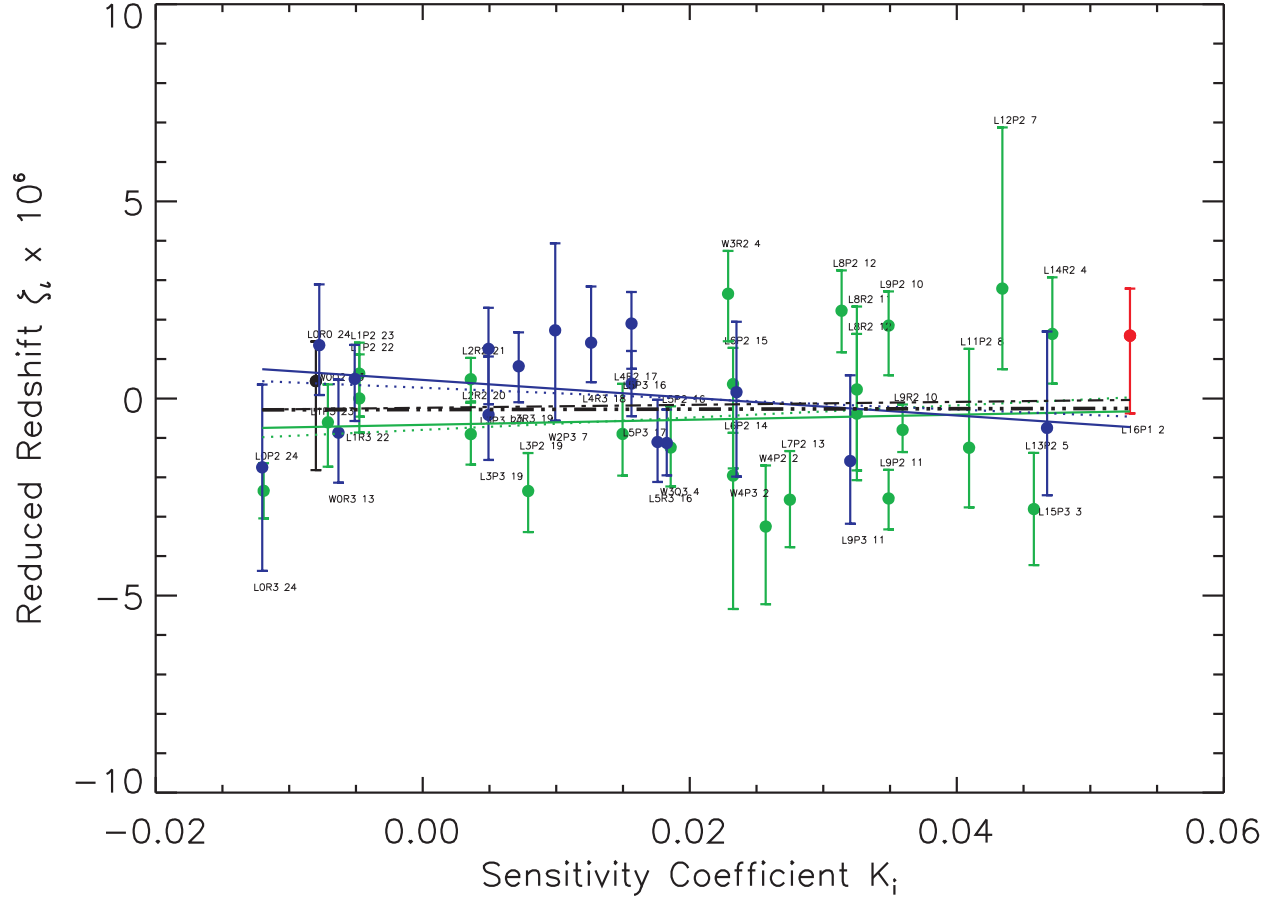


Fig. 6.— Same as Figure 5 except for Q0405-443. In this plot the true order number is 141 minus the printed number.

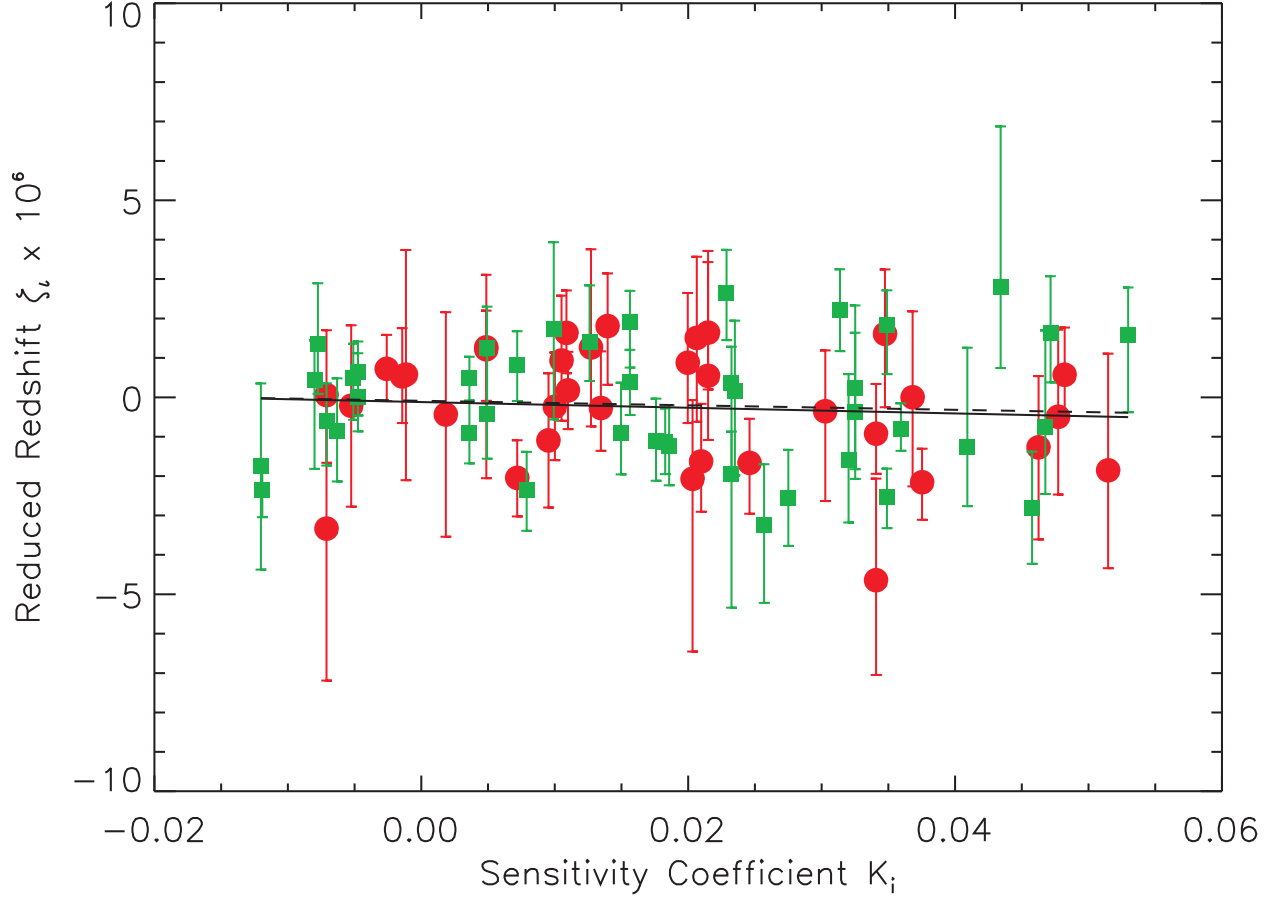


Fig. 7.— The combined data plot of the reduced redshift ζ versus the sensitivity parameter K . The red dots are for Q0347-383 and the green squares are for Q0405-443. The error bars are 1σ . The dashed line is the unweighted fit to the data, $\Delta\mu/\mu = -6 \times 10^{-6} \pm 10. \times 10^{-6}$ and the solid line the weighted fit to the data, $\Delta\mu/\mu = -7 \times 10^{-6} \pm 8 \times 10^{-6}$

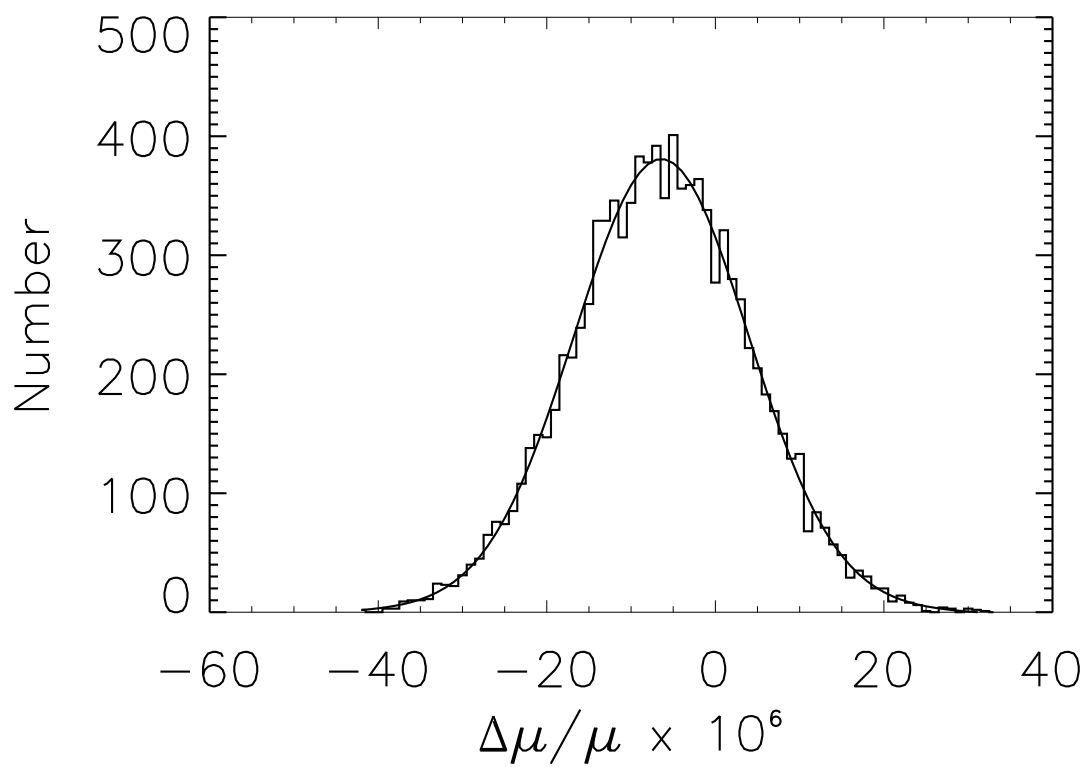


Fig. 8.— The histogram is the output of a 10,000 sample boot strap analysis of the original data. The histogram bins are unity in the units of the abscissa and the ordinate is the number of samples in the bin. The smooth curve is a Gaussian fit to the histogram.

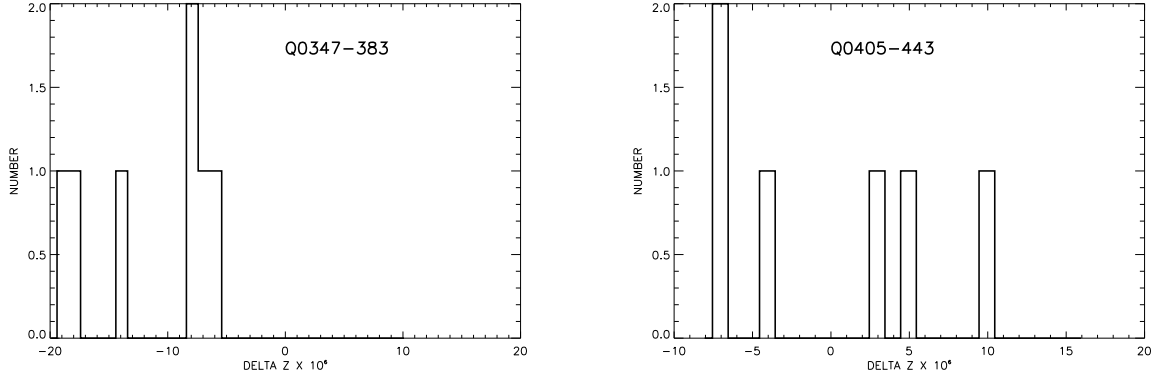


Fig. 9.— Histograms of the delta redshift between each of the Werner band lines and their adjacent Lyman band lines. A positive value means that the Lyman line had a higher redshift than the Werner line. The left histogram is for Q0347-383 and the right is for Q0405-443. Note that this is the delta redshift not the delta reduced redshift defined in Equation 2.